QUARTERLY OF APPLIED MATHEMATICS
VOLUME LXXIV, NUMBER 1
MARCH 2016, PAGES 61–87
http://dx.doi.org/10.1090/qam/1411
Article electronically published on December 3, 2015

A HIGH–ORDER PERTURBATION OF SURFACES (HOPS) APPROACH TO FOKAS INTEGRAL EQUATIONS: THREE–DIMENSIONAL LAYERED–MEDIA SCATTERING

By

DAVID P. NICHOLLS

Department of Mathematics, Statistics, and Computer Science, University of Illinois at Chicago, Chicago, Illinois 60607

Abstract. In this paper we discuss a novel High–Order Perturbation of Surfaces (HOPS) method for the simulation of linear acoustic waves in a three–dimensional layered, periodic structure. The model we consider is that of linear time–harmonic wave propagation which generates three–dimensional, quasiperiodic, outgoing solutions of Helmholtz equations, coupled across irregular layer interfaces. We significantly enhance and stabilize the approach of the author and D. Ambrose, which is a formulation of the problem utilizing the integral equation formalism of Fokas and collaborators. The method is phrased in terms of interfacial variables resulting in a method which has an order of magnitude fewer unknowns than a volumetric approach to this problem. In contrast to classical integral equation formulations, the current contribution does not require specialized quadratures or periodized fundamental solutions. Additionally, as a result of the HOPS philosophy, our new approach is not only faster and better conditioned than the algorithm of the author and Ambrose, it also delivers the scattering returns of an entire family of solutions with a single simulation rather than requiring a new approximation for each profile of interest. Detailed numerical simulations are presented which demonstrate the efficiency, fidelity, and spectral accuracy which can be realized with this new methodology.

1. Introduction. The scattering of linear waves by three dimensional periodic structures is an important phenomena in electromagnetics (e.g., extraordinary optical transmission [12], surface enhanced spectroscopy [26], surface plasmon resonance biosensing [17, 20]), acoustics (e.g., remote sensing [41], nondestructive testing [38], and underwater acoustics [6]), and elastodynamics (e.g., full waveform inversion [5, 42] and hazard assessment [14, 36]). Clearly, the capability to rapidly and robustly simulate such interactions with high accuracy is of fundamental importance to many disciplines.

Received April 25, 2014 and, in revised form, August 12, 2014.
2010 *Mathematics Subject Classification.* Primary 65R20, 65N35.
E-mail address: davidn@uic.edu

In a recent contribution [2] the author and D. Ambrose devised a novel integral equation (IE) formulation of a popular model for such problems based upon the surface formulation of the author [27] and the recent developments of Fokas and collaborators [1, 13, 39, 40]. The resulting numerical method based upon these "Fokas integral equations" (FIE) was shown to be not only rapid and highly accurate, but also quite simple to implement. We build upon this work by showing how a High–Order Perturbation Surfaces (HOPS) methodology which the author has pursued with F. Reitich in [28–30] can be brought to bear upon this problem, yielding a new algorithm with significant enhancements which we outline below.

The most popular approach to these problems (particularly in the engineering literature) are volumetric numerical methods. For instance, from the geosciences literature alone, formulations based upon finite differences (see, e.g., [33]), finite elements (see, e.g., [43]), and spectral elements (see, e.g., [18]) are common. These methods suffer from the requirement that they discretize the full volume of the problem domain, which results in both a prohibitive number of degrees of freedom and also the difficult question of appropriately specifying the far–field boundary condition explicitly.

For these reasons, surface methods are an appealing alternative, particularly those based upon boundary integrals (BIM) or boundary elements (BEM) (see, e.g., [11, 37]). The approach we followed in [2] fell into this category and, as with all BIM/BEM, required only discretization of the layer *interfaces*. Further, due to the choice of Green's function, these BIM/BEM satisfy the far–field boundary condition *exactly*. While these methods can deliver high–accuracy simulations with greatly reduced operation counts, there are several difficulties which need to be addressed [35]. First, high–order simulations can only be realized with specially designed quadrature rules which respect the singularities in Green's function (and its derivative, in certain formulations) [11]. Additionally, BIM/BEM typically give rise to dense linear systems to be solved which require carefully designed preconditioned iterative methods (with accelerated matrix–vector products, e.g., by the Fast–Multipole Method [16]) for configurations of engineering interest [35]. Finally, for periodic structures Green's function must be periodized, which greatly increases the computational cost (see [19] for an exhaustive discussion of this issue).

HOPS methods have emerged as an appealing strategy which maintain the reduced number of degrees of freedom of BIM/BEM while avoiding some of the complications of these latter methods. Among these are the requirement of special quadrature formulas, the need for preconditioned iterative solution procedures for dense systems, and the necessity of periodizing the relevant fundamental solution. The central theme of this contribution is to implement these strategies in the context of the FIE derived in [2]. The original implementations of HOPS methods are: (i) the Method of Field Expansions (Variation of Boundaries) due to Bruno and Reitich [7–9] for doubly layered media and the generalization of Malcolm and Nicholls [22, 27] to multiply–layered structures, and (ii) the Method of Operator Expansions due to Milder [24, 25] (see also improvements in [10]), which was generalized to multiple layers by Malcolm and Nicholls [21, 27]. We also direct the interested reader to the recent SPR simulations using HOPS of Reitich, Johnson, Oh, and Meyer [34] and the author, Reitich, Johnson, and Oh [31].

As we noted in [2], Fokas' approach to deriving integral relations (the FIE referenced above) relating Dirichlet to Neumann data for elliptic boundary value problems yields formulas which do *not* involve the fundamental solution. Instead they feature smooth, "conjugated" solutions of the quasi–periodic Helmholtz problem, meaning that simple quadrature rules (e.g., Nyström's Method [11]) may be utilized while kernel periodization is unnecessary. In addition, due to use of a clever alternative to the standard Green's identity, the *derivative* of the interface shapes never appears in the FIEs, meaning that configurations of rather low smoothness can be accommodated in comparison with alternative approaches.

This new approach cannot avoid the requirement that dense linear systems must be solved to realize a solution. However, we note that in the case of a trivial (flat) interface, these integral operators can be inverted rapidly via the Fast Fourier Transform (FFT) algorithm due to the fact that they are Fourier multipliers [15]. In order to take advantage of this fact for nontrivial deformations we appeal to a HOPS method: The solution in this case is the flat–interface solution plus a correction which can be computed (recursively) to very high order [7, 24, 29]. A particularly appealing feature of FIEs in this context is how *simple* the resulting recursions become, as this amounts to a simple expansion of (complex) exponentials in power series. In addition to the remarkable acceleration of the resulting algorithm (essentially an order of magnitude faster for a low to moderate number of quadrature points and a small number of perturbation orders), two additional benefits of a HOPS approach to this problem which we explore are: (i) the relevant integral operators are much better conditioned in the flat–interface case, and (ii) HOPS methods allow for the solution of problems for entire *families* of configurations by choosing different values of the perturbation parameter.

For the former, as we shall see, our HOPS approach will require the repeated (at every desired perturbation order) solution of a linear system with the *same*, flat–interface operator. This matrix is not only of convolution–type (enabling solution via FFT), but also much better conditioned than the general–interface case. For the latter we will see that our method will deliver the Fourier coefficients, say V_n, in an expansion of the quantity of interest, V, so that we may approximate

$$V(\varepsilon) \approx V^N(\varepsilon) := \sum_{n=0}^{N} V_n \varepsilon^n.$$

For a particular configuration one can simply sum the right–hand side (using one of several alternatives) at the relevant value of ε. However, we note that, with essentially no additional work, V^N can be computed for any number of values of ε (provided they are points of analyticity), thereby obtaining the scattering returns for an entire *family* of structures.

The rest of the paper is organized as follows: In §2 we recall the governing equations of layered media scattering and a convenient surface formulation in §2.1. An implementation of this using FIEs is described in §2.2. A HOPS scheme for simulating these FIEs is outlined in §3 with specific details at order zero given in §3.1, and the general case specified in §3.2. Detailed numerical experiments are presented in §4 with comparisons to exact solutions in §4.3 and layered–media simulations in §4.4. In §4.5 we close with

configurations that are beyond the capabilities of the method outlined in [2] but which can be addressed with our new approach.

2. Governing equations. As we mentioned above, the current contribution presents a significant enhancement to the numerical algorithm presented by the author and D. Ambrose [2] for the simulation of scattering returns by three–dimensional, periodic, layered media. We utilize the same formulation of the problem and, therefore, present only a brief summary of the developments for completeness. We refer the interested reader to [2] for full details.

In this three–dimensional formulation in Cartesian coordinates, $(x, y) = (x_1, x_2, y)$, the laterally $d = (d_1, d_2)$–periodic layered media is specified by (see Figure 1):

(1) Interfaces at

$$y = \bar{g}^{(m)} + g^{(m)}(x_1, x_2) = \bar{g}^{(m)} + g^{(m)}(x), \quad 1 \leq m \leq M,$$

where $x = (x_1, x_2)$, $\bar{g}^{(m)}$ are constants, and

$$g^{(m)}(x + d) = g^{(m)}(x_1 + d_1, x_2 + d_2) = g^{(m)}(x_1, x_2) = g^{(m)}(x),$$

with upward pointing normals $N_m := (-\nabla_x g^{(m)}, 1)^T$.

(2) Constant–density layers (each with constant velocity $c^{(m)}$) specified by

$$\begin{aligned} S^{(0)} &:= \left\{ y > \bar{g}^{(1)} + g^{(1)}(x) \right\} \\ S^{(m)} &:= \left\{ \bar{g}^{(m+1)} + g^{(m+1)}(x) < y < \bar{g}^{(m)} + g^{(m)}(x) \right\}, \qquad 1 \leq m \leq M-1 \\ S^{(M)} &:= \left\{ y < \bar{g}^{(M)} + g^{(M)}(x) \right\}. \end{aligned}$$

Each layer has wavenumber $k^{(m)} := \omega / c^{(m)}$, which characterizes the properties of the material and the frequency of radiation.

(3) Plane–wave insonification from above specified by

$$u^{inc}(x, y, t) = e^{-i\omega t} e^{i(\alpha \cdot x - \beta y)} =: e^{-i\omega t} v^{inc}(x, y), \quad \alpha = (\alpha_1, \alpha_2)^T.$$

This time–dependent problem can be restated as a time–harmonic one of time–independent *reduced* scattered fields, $v^{(m)}(x, y)$, which, in each layer, are α–quasiperiodic [32]:

$$v^{(m)}(x + d, y) = e^{i(\alpha \cdot d)} v^{(m)}(x, y).$$

These fields each satisfy a Helmholtz equation

$$\Delta v^{(m)} + (k^{(m)})^2 v^{(m)} = 0, \quad \text{in } S^{(m)}, \quad 0 \leq m \leq M,$$

and for the incident radiation to be a solution we have $|\alpha|^2 + \beta^2 = (k^{(0)})^2$. At the material interfaces the fields are coupled through Dirichlet and Neumann boundary conditions:

$$v^{(m-1)} - v^{(m)} = \zeta^{(m)}, \qquad \text{at } y = \bar{g}^{(m)} + g^{(m)}(x), \quad 1 \leq m \leq M, \tag{2.1a}$$

$$\partial_{N^{(m)}} \left[v^{(m-1)} - v^{(m)} \right] = \psi^{(m)}, \qquad \text{at } y = \bar{g}^{(m)} + g^{(m)}(x), \quad 1 \leq m \leq M, \tag{2.1b}$$

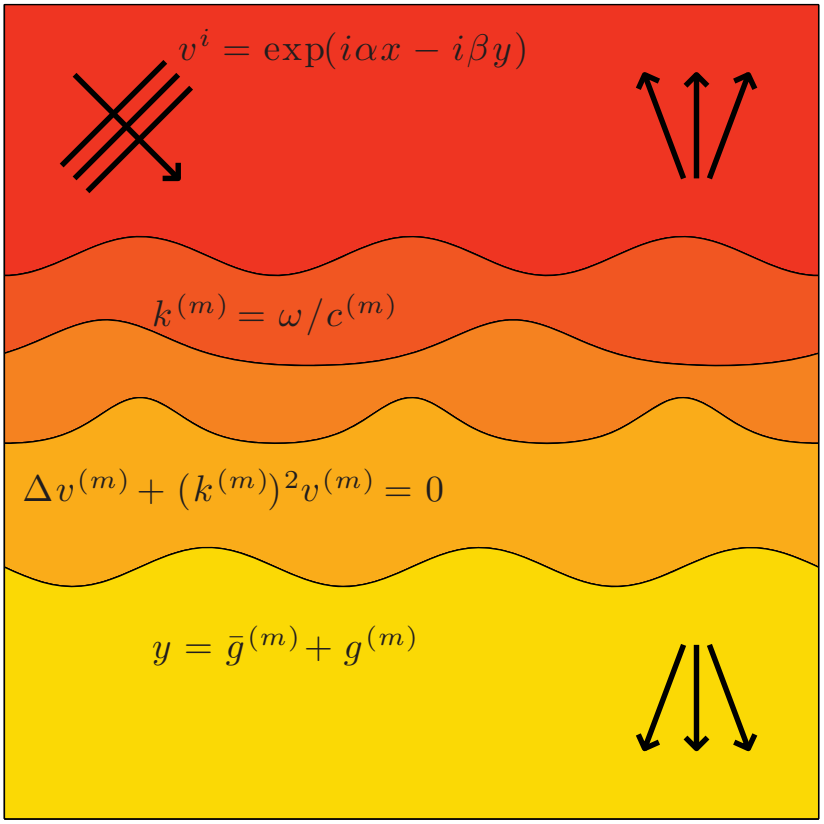

FIG. 1. Depiction of a multiply layered media insonified from above by plane–wave radiation.

$\partial_{N^{(m)}} := N^{(m)} \cdot \nabla$. In the case of insonification from above

$$\begin{aligned}
\zeta^{(1)} &= -v^{inc}(x, \bar{g}^{(1)} + g^{(1)}(x)) \\
\psi^{(1)} &= -(\partial_{N^{(1)}} v^{inc})(x, \bar{g}^{(1)} + g^{(1)}(x)) \\
\zeta^{(m)} &\equiv 0 \qquad\qquad 2 \le m \le M \\
\psi^{(m)} &\equiv 0 \qquad\qquad 2 \le m \le M.
\end{aligned}$$

Finally, outgoing wave conditions are enforced on $v^{(0)}$ and $v^{(M)}$ at positive and negative infinity, respectively.

2.1. *Boundary formulation.* To recall the boundary formulation of [2] we define the (lower and upper) Dirichlet traces:

$$\begin{aligned}
V^{(m),l}(x) &:= v^{(m)}(x, \bar{g}^{(m+1)} + g^{(m+1)}(x)) \qquad 0 \le m \le M-1 \\
V^{(m),u}(x) &:= v^{(m)}(x, \bar{g}^{(m)} + g^{(m)}(x)) \qquad 1 \le m \le M,
\end{aligned}$$

and the (lower and upper) exterior Neumann traces:

$$\tilde{V}^{(m),l}(x) := -(\partial_{N^{(m+1)}} v^{(m)})(x, \bar{g}^{(m+1)} + g^{(m+1)}(x)) \qquad 0 \leq m \leq M-1$$
$$\tilde{V}^{(m),u}(x) := (\partial_{N^{(m)}} v^{(m)})(x, \bar{g}^{(m)} + g^{(m)}(x)) \qquad 1 \leq m \leq M.$$

We further recall the integral relations which couple the Dirichlet and Neumann traces (through the solution of the relevant Helmholtz equations) [2]:

$$A(0)\tilde{V}^{(0),l} - R(0)V^{(0),l} = 0, \tag{2.2a}$$
$$\begin{pmatrix} A^{uu}(m) & A^{ul}(m) \\ A^{lu}(m) & A^{ll}(m) \end{pmatrix} \begin{pmatrix} \tilde{V}^{(m),u} \\ \tilde{V}^{(m),l} \end{pmatrix} - \begin{pmatrix} R^{uu}(m) & R^{ul}(m) \\ R^{lu}(m) & R^{ll}(m) \end{pmatrix} \begin{pmatrix} V^{(m),u} \\ V^{(m),l} \end{pmatrix} = \begin{pmatrix} 0 \\ 0 \end{pmatrix}, \tag{2.2b}$$
$$1 \leq m \leq M-1,$$
$$A(M)\tilde{V}^{(M),u} - R(M)V^{(M),u} = 0. \tag{2.2c}$$

In terms of the Dirichlet and Neumann traces, and using the integral relations above, the author and Ambrose showed [2] that the layered media scattering problem is equivalent to

$$\mathbf{M}\mathbf{V}^{(\mathbf{l})} = \mathbf{Q} \tag{2.3}$$

where

$$\mathbf{M} := \begin{pmatrix} A(0) & -R(0) & 0 & & \cdots & 0 \\ -A^{uu}(1) & -R^{uu}(1) & A^{ul}(1) & -R^{ul}(1) & \cdots & 0 \\ -A^{lu}(1) & -R^{lu}(1) & A^{ll}(1) & -R^{ll}(1) & \cdots & 0 \\ \vdots & & & & & \vdots \\ 0 & \cdots & -A^{uu}(M-1) & -R^{uu}(M-1) & A^{ul}(M-1) & -R^{ul}(M-1) \\ 0 & \cdots & -A^{lu}(M-1) & -R^{lu}(M-1) & A^{ll}(M-1) & -R^{ll}(M-1) \\ 0 & \cdots & & 0 & -A(M) & -R(M) \end{pmatrix}$$

and

$$\mathbf{V}^{(\mathbf{l})} := \begin{pmatrix} \tilde{V}^{(0),l} \\ V^{(0),l} \\ \vdots \\ \tilde{V}^{(M-1),l} \\ V^{(M-1),l} \end{pmatrix}, \quad \mathbf{Q} := \begin{pmatrix} 0 \\ A^{uu}(1)\psi^{(1)} - R^{uu}(1)\zeta^{(1)} \\ A^{lu}(1)\psi^{(1)} - R^{lu}(1)\zeta^{(1)} \\ \vdots \\ A^{uu}(M-1)\psi^{(M-1)} - R^{uu}(M-1)\zeta^{(M-1)} \\ A^{lu}(M-1)\psi^{(M-1)} - R^{lu}(M-1)\zeta^{(M-1)} \\ A(M)\psi^{(M)} - R(M)\zeta^{(M)} \end{pmatrix}.$$

2.2. *Fokas integral equations.* In [2] we showed that the operators in (2.2) can all be stated generically as

$$\hat{A}_p \left[\tilde{V}\right] = \hat{R}_p [V], \quad p \in \mathbf{Z}, \tag{2.4}$$

and we term the approximation of these by Nyström's method the "Direct Method" of [2]. More specifically, in the top layer, if

$$\tilde{V} = G, \quad V = \xi, \quad g^{(1)}(x) = g(x),$$

then (abbreviating the double integral over $[0,d_1]\times[0,d_2]$ by $\int_0^d$) we have

$$\hat{A}_p(g)\,[G] = \int_0^d e^{i\beta_p^{(0)}g} e^{-i\alpha_p\cdot x} G(x)\,dx, \tag{2.5a}$$

$$\hat{R}_p(g)\,[\xi] = \int_0^d e^{i\beta_p^{(0)}g} e^{-i\alpha_p\cdot x} \left\{ \frac{i\alpha_p}{i\beta_p^{(0)}}\cdot\nabla_x + \frac{(k^{(0)})^2}{i\beta_p^{(0)}} \right\} \xi(x)\,dx, \tag{2.5b}$$

where, for $m=0,\dots,M$,

$$\alpha_p := \begin{pmatrix} \alpha_1 + 2\pi p_1/d_1 \\ \alpha_2 + 2\pi p_2/d_2 \end{pmatrix}, \quad \beta_p^{(m)} := \begin{cases} \sqrt{(k^{(m)})^2 - |\alpha_p|^2} & p\in\mathcal{U}^{(m)} \\ i\sqrt{|\alpha_p|^2 - (k^{(m)})^2} & p\notin\mathcal{U}^{(m)}, \end{cases}$$

and the set of propagating modes are

$$\mathcal{U}^{(m)} := \left\{ p \mid |\alpha_p|^2 < (k^{(m)})^2 \right\}.$$

We point out that if we specify the Dirichlet data $V=\xi$, then solving for $\tilde{V}=G$ produces the output of the Dirichlet–Neumann operator (DNO).

In the bottom layer, if

$$\tilde{V} = J, \quad V = \zeta, \quad g^{(M)}(x) = g(x),$$

then

$$\hat{A}_p(g)\,[J] = \int_0^d e^{-i\beta_p^{(M)}g} e^{-i\alpha_p\cdot x} J(x)\,dx, \tag{2.6a}$$

$$\hat{R}_p(g)\,[\zeta] = \int_0^d e^{-i\beta_p^{(M)}g} e^{-i\alpha_p\cdot x} \left\{ \frac{i\alpha_p}{i\beta_p^{(M)}}\cdot\nabla_x + \frac{(k^{(M)})^2}{i\beta_p^{(M)}} \right\} \zeta(x)\,dx. \tag{2.6b}$$

Finally, in a middle layer, if

$$\tilde{V} = \begin{pmatrix} \tilde{V}^u \\ \tilde{V}^\ell \end{pmatrix} = \begin{pmatrix} U \\ L \end{pmatrix}, \quad V = \begin{pmatrix} V^u \\ V^\ell \end{pmatrix} = \begin{pmatrix} \zeta \\ \xi \end{pmatrix},$$
$$\bar{g}^{(m)} = \bar{u}, \quad \bar{g}^{(m+1)} = \bar{\ell}, \quad g^{(m)}(x) = u(x), \quad g^{(m+1)}(x) = \ell(x),$$

then

$$\hat{A}_p(u,\ell)\left[\begin{pmatrix} U \\ L \end{pmatrix}\right] = \int_0^d \begin{pmatrix} C(u) + \mathrm{co}_p\, S(u) & \mathrm{cs}_p\, S(\ell) \\ -\mathrm{cs}_p\, S(u) & C(\ell) - \mathrm{co}_p\, S(\ell) \end{pmatrix} \begin{pmatrix} U \\ L \end{pmatrix} e^{-i\alpha_p\cdot x}\,dx, \tag{2.7a}$$

$$\hat{R}_p(u,\ell)\left[\begin{pmatrix} \zeta \\ \xi \end{pmatrix}\right] = \int_0^d \begin{pmatrix} -\mathrm{co}_p\, C(u) - S(u) & \mathrm{cs}_p\, C(\ell) \\ \mathrm{cs}_p\, C(u) & -\mathrm{co}_p\, C(\ell) + S(\ell) \end{pmatrix}, \tag{2.7b}$$

$$\times \left\{ \frac{i\alpha_p}{i\beta_p^{(m)}}\cdot\nabla_x + \frac{(k^{(m)})^2}{i\beta_p^{(m)}} \right\} \begin{pmatrix} \zeta \\ \xi \end{pmatrix} e^{-i\alpha_p\cdot x}\,dx, \tag{2.7c}$$

where

$$\mathrm{co}_p := \coth(i\beta_p^{(m)}(\bar{u}-\bar{\ell})), \quad \mathrm{cs}_p := \mathrm{csch}(i\beta_p^{(m)}(\bar{u}-\bar{\ell})),$$
$$C(u) := \cosh(i\beta_p^{(m)}u), \quad S(u) := \sinh(i\beta_p^{(m)}u),$$
$$C(\ell) := \cosh(i\beta_p^{(m)}\ell), \quad S(\ell) := \sinh(i\beta_p^{(m)}\ell).$$

3. A High–Order Perturbation of Surfaces (HOPS) method. At this point we depart from the methodology of [2] and, rather than simply enforcing the equations (2.4) directly using, e.g., Nyström's method [11], we recognize that these FIEs depend upon the boundary perturbation (e.g., g in (2.5)) in a rather simple way. In fact, considering (2.5), if we set $g(x) = \varepsilon f(x)$, then the integral operators $\hat{A}_p$ and $\hat{R}_p$ depend *analytically* upon ε (sufficiently small) so that, e.g.,

$$\hat{A}_p(g) = \hat{A}_p(\varepsilon f) = \sum_{n=0}^{\infty} \hat{A}_{p,n}(f)\varepsilon^n, \quad \hat{R}_p(g) = \hat{R}_p(\varepsilon f) = \sum_{n=0}^{\infty} \hat{R}_{p,n}(f)\varepsilon^n. \tag{3.1}$$

In light of these expansions one can posit the forms

$$V(g) = V(\varepsilon f) = \sum_{n=0}^{\infty} V_n(f)\varepsilon^n, \quad \tilde{V}(g) = \tilde{V}(\varepsilon f) = \sum_{n=0}^{\infty} \tilde{V}_n(f)\varepsilon^n. \tag{3.2}$$

In particular, for the problem of computing a Dirichlet–Neumann operator [28–30], given analytic Dirichlet data (so that the first expansion in (3.2) converges strongly), we fully anticipate that the corresponding Neumann data will also be analytic [28] so that the second expansion is also valid.

If we insert the expansions (3.1) and (3.2) into (2.4), this results in

$$\left(\sum_{n=0}^{\infty} \hat{A}_{p,n}\varepsilon^n\right)\left[\sum_{m=0}^{\infty} \tilde{V}_m\varepsilon^m\right] = \left(\sum_{n=0}^{\infty} \hat{R}_{p,n}\varepsilon^n\right)\left[\sum_{m=0}^{\infty} V_m\varepsilon^m\right].$$

This, evidently regular, perturbation expansion can now be equated at successive orders of ε delivering,

$$\hat{A}_{p,0}\left[\tilde{V}_n\right] = \hat{R}_{p,0}\left[V_n\right] + \sum_{m=0}^{n-1} \hat{R}_{p,n-m}\left[V_m\right] - \sum_{m=0}^{n-1} \hat{A}_{p,n-m}\left[\tilde{V}_m\right]. \tag{3.3}$$

This recursion describes a natural HOPS scheme for the simulation of quantities of interest which is advantaged over (2.4) in a number of ways.

First, the solution of (2.4) requires the formation and inversion of $\hat{A}_p(g)$, which, as we shall show, can become quite *ill–conditioned* as the boundary deformation g departs significantly from zero. By contrast, in solving (3.3) one must (repeatedly) invert the operator $\hat{A}_{p,0} = \hat{A}_p(0)$, which, as we will see, is both *well–conditioned* and can be accomplished *rapidly* using the FFT algorithm.

Second, one may perceive that a disadvantage of utilizing (3.3) is that this system must be solved at every perturbation order n desired, which would make it much more computationally intensive than inverting (2.4) once. However, this is, in fact, a *strength*, as it allows one to compute the Neumann data for an entire *family* of profiles $g(x) = \varepsilon f(x)$ with one simulation. That is, upon solving (3.3) for $0 \leq n \leq N$, we can form

$$\tilde{V}^N(x;\varepsilon) := \sum_{n=0}^{N} \tilde{V}_n(x)\varepsilon^n \tag{3.4}$$

and approximate $\tilde{V}$ corresponding to $g = \varepsilon f$ for *any* ε by a simple summation (with linear cost). By contrast, if one wished to do the same with (2.4), the operator $\hat{A}_p(g)$ must be formed and inverted with every new instance of g.

At this point we simply require forms for the Taylor coefficients of the integral operators $\hat{A}_p$ and $\hat{R}_p$, namely $\{\hat{A}_{p,n}, \hat{R}_{n,p}\}$. As we now show, the matter is a simple one, and, in fact, in [2] we identified the "flat interface" operators $\{\hat{A}_{p,0}, \hat{R}_{p,0}\}$ explicitly (though we made no particular use of them). We reproduce that simple analysis in the next subsection.

3.1. *Flat interfaces.* In the class of flat interfaces ($g \equiv 0$, $u \equiv 0$, $\ell \equiv 0$) we have, in the top layer (2.5),

$$\hat{A}_p(0)\,[G] = \int_0^d e^{-i\alpha_p\cdot x} G(x)\,dx, \tag{3.5a}$$

$$\hat{R}_p(0)\,[\xi] = \int_0^d e^{-i\alpha_p\cdot x} \left\{ \frac{i\alpha_p}{i\beta_p^{(0)}}\cdot\nabla_x + \frac{(k^{(0)})^2}{i\beta_p^{(0)}} \right\} \xi(x)\,dx, \tag{3.5b}$$

in the bottom layer

$$\hat{A}_p(0)\,[J] = \int_0^d e^{-i\alpha_p\cdot x} J(x)\,dx, \tag{3.6a}$$

$$\hat{R}_p(0)\,[\zeta] = \int_0^d e^{-i\alpha_p\cdot x} \left\{ \frac{i\alpha_p}{i\beta_p^{(M)}}\cdot\nabla_x + \frac{(k^{(M)})^2}{i\beta_p^{(M)}} \right\} \zeta(x)\,dx, \tag{3.6b}$$

and in the middle layers

$$\hat{A}_p(0,0)\left[\begin{pmatrix} U \\ L \end{pmatrix}\right] = \int_0^d \begin{pmatrix} 1 & 0 \\ 0 & 1 \end{pmatrix} \begin{pmatrix} U \\ L \end{pmatrix} e^{-i\alpha_p\cdot x}\,dx, \tag{3.7a}$$

$$\hat{R}_p(0,0)\left[\begin{pmatrix} \zeta \\ \xi \end{pmatrix}\right] = \int_0^d \begin{pmatrix} -\operatorname{co}_p & \operatorname{cs}_p \\ \operatorname{cs}_p & -\operatorname{co}_p \end{pmatrix} \left\{ \frac{i\alpha_p}{i\beta_p^{(m)}}\cdot\nabla_x + \frac{(k^{(m)})^2}{i\beta_p^{(m)}} \right\} \begin{pmatrix} \zeta \\ \xi \end{pmatrix} e^{-i\alpha_p\cdot x}\,dx. \tag{3.7b}$$

Recognizing the Fourier transform

$$\hat{\psi}_p = \mathcal{F}\,[\psi] = \int_0^d e^{-i\alpha_p\cdot x}\psi(x)\,dx$$

and using the fact that $(i\alpha_p)\cdot(i\alpha_p) + (k^{(m)})^2 = -(i\beta_p^{(m)})^2$, we find in the top layer

$$\hat{A}_p(0)\,[G] = \hat{G}_p$$

$$\hat{R}_p(0)\,[\xi] = \left\{ \frac{i\alpha_p}{i\beta_p^{(0)}}\cdot(i\alpha_p) + \frac{(k^{(0)})^2}{i\beta_p^{(0)}} \right\} \hat{\xi}_p = -(i\beta_p^{(0)})\hat{\xi}_p,$$

in the bottom layer

$$\hat{A}_p(0)\,[J] = \hat{J}_p$$

$$\hat{R}_p(0)\,[\zeta] = \left\{ \frac{i\alpha_p}{i\beta_p^{(M)}}\cdot(i\alpha_p) + \frac{(k^{(M)})^2}{i\beta_p^{(M)}} \right\} \hat{\zeta}_p = -(i\beta_p^{(M)})\hat{\zeta}_p,$$

and in the middle layer

$$\hat{A}_p(0,0)\left[\begin{pmatrix} U \\ L \end{pmatrix}\right] = \begin{pmatrix} 1 & 0 \\ 0 & 1 \end{pmatrix}\begin{pmatrix} \hat{U}_p \\ \hat{L}_p \end{pmatrix}$$

$$\hat{R}_p(0,0)\left[\begin{pmatrix} \zeta \\ \xi \end{pmatrix}\right] = \begin{pmatrix} -\operatorname{co}_p & \operatorname{cs}_p \\ \operatorname{cs}_p & -\operatorname{co}_p \end{pmatrix}\left\{\frac{i\alpha_p}{i\beta_p^{(m)}}\cdot(i\alpha_p) + \frac{(k^{(m)})^2}{i\beta_p^{(m)}}\right\}\begin{pmatrix} \hat{\zeta}_p \\ \hat{\xi}_p \end{pmatrix}$$

$$= \begin{pmatrix} -\operatorname{co}_p & \operatorname{cs}_p \\ \operatorname{cs}_p & -\operatorname{co}_p \end{pmatrix}(-i\beta_p^{(m)})\begin{pmatrix} \hat{\zeta}_p \\ \hat{\xi}_p \end{pmatrix}.$$

From these we recover the classical flat–interface results

$$\hat{G}_p = -(i\beta_p^{(0)})\hat{\xi}_p, \quad \hat{J}_p = -(i\beta_p^{(M)})\hat{\zeta}_p, \quad \begin{pmatrix} \hat{U}_p \\ \hat{L}_p \end{pmatrix} = (i\beta_p^{(m)})\begin{pmatrix} \operatorname{co}_p & -\operatorname{cs}_p \\ -\operatorname{cs}_p & \operatorname{co}_p \end{pmatrix}\begin{pmatrix} \hat{\zeta}_p \\ \hat{\xi}_p \end{pmatrix}.$$

3.2. *Higher–order corrections.* Based on the forms for (2.5), (2.6), and (2.7), it is straightforward to compute the $\hat{A}_{p,n}$ and $\hat{R}_{p,n}$. In particular, for the upper layer, if $g(x) = \varepsilon f(x)$, then (2.5) gives

$$\hat{A}_{p,n}(f)\,[G] = \int_0^d (i\beta_p^{(0)})^n F_n(x) e^{-i\alpha_p\cdot x} G(x)\,dx, \tag{3.8a}$$

$$\hat{R}_{p,n}(f)\,[\xi] = \int_0^d (i\beta_p^{(0)})^n F_n(x) e^{-i\alpha_p\cdot x}\left\{\frac{i\alpha_p}{i\beta_p^{(0)}}\cdot\nabla_x + \frac{(k^{(0)})^2}{i\beta_p^{(0)}}\right\}\xi(x)\,dx, \tag{3.8b}$$

where $F_n(x) := f(x)^n/n!$. In the lower layer, if $g(x) = \varepsilon f(x)$, then (2.6) gives

$$\hat{A}_{p,n}(f)\,[J] = \int_0^d (-i\beta_p^{(M)})^n F_n(x) e^{-i\alpha_p\cdot x} J(x)\,dx, \tag{3.9a}$$

$$\hat{R}_{p,n}(f)\,[\zeta] = \int_0^d (-i\beta_p^{(M)})^n F_n(x) e^{-i\alpha_p\cdot x}\left\{\frac{i\alpha_p}{i\beta_p^{(M)}}\cdot\nabla_x + \frac{(k^{(M)})^2}{i\beta_p^{(M)}}\right\}\zeta(x)\,dx. \tag{3.9b}$$

Finally, in a middle layer, if $u(x) = \varepsilon f_u(x)$ and $\ell(x) = \varepsilon f_\ell(x)$, then (2.7) delivers

$$\hat{A}_{p,n}(f_u, f_\ell)\left[\begin{pmatrix} U \\ L \end{pmatrix}\right] = \int_0^d \begin{pmatrix} (C_n + \operatorname{co}_p S_n)F_{u,n} & \operatorname{cs}_p S_n F_{\ell,n} \\ -\operatorname{cs}_p S_n F_{u,n} & (C_n - \operatorname{co}_p S_n)F_{\ell,n} \end{pmatrix}\begin{pmatrix} U \\ L \end{pmatrix} e^{-i\alpha_p\cdot x}\,dx, \tag{3.10a}$$

$$\hat{R}_{p,n}(f_u, f_\ell)\left[\begin{pmatrix} \zeta \\ \xi \end{pmatrix}\right] = \int_0^d \begin{pmatrix} (-\operatorname{co}_p C_n - S_n)F_{u,n} & \operatorname{cs}_p C_n F_{\ell,n} \\ \operatorname{cs}_p C_n F_{u,n} & (-\operatorname{co}_p C_n + S_n)F_{\ell,n} \end{pmatrix} \times\left\{\frac{i\alpha_p}{i\beta_p^{(m)}}\cdot\nabla_x + \frac{(k^{(m)})^2}{i\beta_p^{(m)}}\right\}\begin{pmatrix} \zeta \\ \xi \end{pmatrix} e^{-i\alpha_p\cdot x}\,dx, \tag{3.10b}$$

where

$$F_{u,n} := (f_u(x))^n/n!, \quad F_{\ell,n} := (f_\ell(x))^n/n!,$$

and, for $j = 0, 1, \ldots,$

$$C_{2j} := (i\beta_p^{(m)})^{2j}, \quad C_{2j+1} := 0, \quad S_{2j} := 0, \quad S_{2j+1} := (i\beta_p^{(m)})^{2j+1}.$$

At this point we are able to make a *crucial* observation which gives an unexpected *computational* benefit to our approach as opposed to the one advanced in [2]. Specifically,

we note that in (3.8), (3.9), and (3.10) we are able to separate the wavenumber (p) dependence from the spatial (x) dependence in the following ways. For (3.8) we write

$$\hat{A}_{p,n}(f)\,[G] = (i\beta_p^{(0)})^n \int_0^d e^{-i\alpha_p\cdot x} F_n(x) G(x)\,dx, \tag{3.11a}$$

$$\begin{aligned}\hat{R}_{p,n}(f)\,[\xi] &= (i\beta_p^{(0)})^n \left(\frac{i\alpha_p}{i\beta_p^{(0)}}\right)\cdot \int_0^d e^{-i\alpha_p\cdot x} F_n(x)\nabla_x\xi(x)\,dx \\ &\quad + (i\beta_p^{(0)})^n \left(\frac{(k^{(0)})^2}{i\beta_p^{(0)}}\right)\int_0^d e^{-i\alpha_p\cdot x} F_n(x)\xi(x)\,dx.\end{aligned} \tag{3.11b}$$

For (3.9)

$$\hat{A}_{p,n}(f)\,[J] = (-i\beta_p^{(M)})^n \int_0^d e^{-i\alpha_p\cdot x} F_n(x) J(x)\,dx, \tag{3.12a}$$

$$\begin{aligned}\hat{R}_{p,n}(f)\,[\xi] &= (-i\beta_p^{(M)})^n \left(\frac{i\alpha_p}{i\beta_p^{(M)}}\right)\cdot \int_0^d e^{-i\alpha_p\cdot x} F_n(x)\nabla_x\zeta(x)\,dx \\ &\quad + (-i\beta_p^{(M)})^n \left(\frac{(k^{(M)})^2}{i\beta_p^{(M)}}\right)\int_0^d e^{-i\alpha_p\cdot x} F_n(x)\zeta(x)\,dx.\end{aligned} \tag{3.12b}$$

Finally, for (3.10) we can state that

$$\hat{A}_{p,n}(f_u, f_\ell)\left[\begin{pmatrix} U \\ L\end{pmatrix}\right] = \begin{pmatrix} C_n + \mathrm{co}_p\, S_n & \mathrm{cs}_p\, S_n \\ -\mathrm{cs}_p\, S_n & C_n - \mathrm{co}_p\, S_n\end{pmatrix}\int_0^d e^{-i\alpha_p\cdot x}\begin{pmatrix} F_{u,n}U \\ F_{\ell,n}L\end{pmatrix}\,dx, \tag{3.13a}$$

$$\begin{aligned}\hat{R}_{p,n}(f_u, f_\ell)\left[\begin{pmatrix}\zeta \\ \xi\end{pmatrix}\right] &= \begin{pmatrix} -\mathrm{co}_p\, C_n - S_n & \mathrm{cs}_p\, C_n \\ \mathrm{cs}_p\, C_n & -\mathrm{co}_p\, C_n + S_n\end{pmatrix}\begin{pmatrix}\dfrac{i\alpha_p}{i\beta_p^{(m)}}\end{pmatrix} \\ &\quad \cdot \int_0^d e^{-i\alpha_p\cdot x}\begin{pmatrix} F_{u,n}\nabla_x\zeta \\ F_{\ell,n}\nabla_x\xi\end{pmatrix}\,dx \\ &\quad + \begin{pmatrix} -\mathrm{co}_p\, C_n - S_n & \mathrm{cs}_p\, C_n \\ \mathrm{cs}_p\, C_n & -\mathrm{co}_p\, C_n + S_n\end{pmatrix}\left(\frac{(k^{(m)})^2}{i\beta_p^{(m)}}\right)\int_0^d e^{-i\alpha_p\cdot x}\begin{pmatrix} F_{u,n}\zeta \\ F_{\ell,n}\xi\end{pmatrix}\,dx.\end{aligned} \tag{3.13b}$$

The important observation to make about all of these is that they are convolution operators which can be rapidly evaluated by the FFT algorithm. For instance, in using (3.11) one could perform the following sequence of steps to evaluate the *action* of $\hat{A}_{n,p}$ on the function $G(x)$ evaluated at N_x equally–spaced points on $[0, d]$:

(1) Multiply $G(x)$ by $F_n(x)$ pointwise in "physical space" (Cost: $\mathcal{O}(N_x)$).
(2) Fourier transform the product via the FFT (Cost: $\mathcal{O}(N_x \log(N_x))$).
(3) Multiply pointwise by the diagonal operator $(i\beta_p^{(0)})^n$ in "Fourier space" (Cost: $\mathcal{O}(N_x)$).

We point out that, at this point, it is quite natural to move back to "physical space" by inverse Fourier transform. We use this convention for the rest of this contribution, which amounts to replacing (3.3) by

$$A_0\left[\tilde{V}_n\right] = R_0\,[V_n] + \sum_{m=0}^{n-1} R_{n-m}\,[V_m] - \sum_{m=0}^{n-1} A_{n-m}\left[\tilde{V}_m\right], \tag{3.14}$$

where

$$A_n = \frac{1}{|d|}\sum_{p=-\infty}^{\infty} \hat{A}_{p,n} e^{i\alpha_p \cdot \tilde{x}}, \quad R_n = \frac{1}{|d|}\sum_{p=-\infty}^{\infty} \hat{R}_{p,n} e^{i\alpha_p \cdot \tilde{x}}.$$

3.3. *Computing far–field information: The efficiencies.* In periodic layered media scattering the "far field" information is encoded in the efficiencies [32], and in this section we describe a simple approach to garnering this information in our current formulation.

We start by recalling the Rayleigh expansions [32], which state that above the structure $(y > \bar{g}^{(1)} + \left|g^{(1)}\right|_{L^\infty})$ the scattered field can be expressed as

$$v^{(0)}(x,y) = \sum_{p=-\infty}^{\infty} B_p^{(0)} e^{i\alpha_p \cdot x + i\beta_p^{(0)} y}, \tag{3.15}$$

while below the structure $(y < \bar{g}^{(M)} - \left|g^{(M)}\right|_{L^\infty})$,

$$v^{(M)}(x,y) = \sum_{p=-\infty}^{\infty} B_p^{(M)} e^{i\alpha_p \cdot x - i\beta_p^{(M)} y}.$$

The upper and lower efficiencies are defined by

$$e_p^{(0)} := \frac{\beta_p^{(0)}}{\beta}\left|B_p^{(0)}\right|^2, \qquad p \in \mathcal{U}^{(0)}, \tag{3.16a}$$

$$e_p^{(M)} := \frac{\beta_p^{(M)}}{\beta}\left|B_p^{(M)}\right|^2, \qquad p \in \mathcal{U}^{(M)}. \tag{3.16b}$$

At a plane $y = \bar{a} > \bar{g}^{(1)} + \left|g^{(1)}\right|_{L^\infty}$ the Rayleigh expansion (3.15) is *exact*, so that if one of our problem unknowns is $U(x) := v^{(0)}(x,\bar{a})$, then

$$\sum_{p=-\infty}^{\infty} \hat{U}_p e^{i\alpha_p \cdot x} = U(x) = v^{(0)}(x,\bar{a}) = \sum_{p=-\infty}^{\infty} B_p^{(0)} e^{i\alpha_p \cdot x + i\beta_p^{(0)}\bar{a}},$$

so that

$$B_p^{(0)} = \hat{U}_p e^{-i\beta_p^{(0)}\bar{a}}, \tag{3.17}$$

and the efficiencies are simple to compute from (3.16). Of course the same considerations at $y = -\bar{b} < \bar{g}^{(M)} - \left|g^{(M)}\right|_{L^\infty}$ coupled to (3.3) yield, for $W(x) := v^{(M)}(x,-\bar{b})$,

$$B_p^{(M)} = \hat{W}_p e^{-i\beta_p^{(M)}\bar{b}}. \tag{3.18}$$

Therefore, if we always choose two flat "artificial" boundaries (the material properties are the *same* on both sides) away from the structure, then the efficiencies can be trivially estimated from (3.17) and (3.18).

REMARK 3.1. There is a principle of conservation of energy for lossless media which states that

$$\sum_{p\in\mathcal{U}^{(0)}} e_p^{(0)} + \sum_{p\in\mathcal{U}^{(M)}} e_p^{(M)} = 1,$$

which gives a diagnostic of convergence, the "energy defect"

$$\delta := 1 - \sum_{p\in\mathcal{U}^{(0)}} e_p^{(0)} - \sum_{p\in\mathcal{U}^{(M)}} e_p^{(M)}. \tag{3.19}$$

4. Numerical results. At this point we are in a position to present results of numerical simulations conducted with our new algorithm. As we mentioned above, the scheme is simply Nyström's method applied to each of the integral equations (3.14) which appear in the full layered–medium system (2.3).

4.1. *Exact solutions.* Once again, following the developments of [2], we observe that, in building a numerical solver for a *homogeneous* PDE and boundary conditions

$$\begin{aligned} \mathcal{L}u &= 0 && \text{in } \Omega \\ \mathcal{B}u &= 0 && \text{at } \partial\Omega, \end{aligned}$$

it is often just as easy to construct an algorithm for the corresponding *inhomogeneous* problem:

$$\begin{aligned} \mathcal{L}u &= \mathcal{R} && \text{in } \Omega \\ \mathcal{B}u &= \mathcal{Q} && \text{at } \partial\Omega. \end{aligned}$$

Selecting an arbitrary function w, we can compute

$$\mathcal{R}_w := \mathcal{L}w, \quad \mathcal{Q}_w := \mathcal{B}w,$$

and now have an *exact* solution to the problem

$$\begin{aligned} \mathcal{L}u &= \mathcal{R}_w && \text{in } \Omega \\ \mathcal{B}u &= \mathcal{Q}_w && \text{at } \partial\Omega, \end{aligned}$$

namely $u = w$. In this way we can test our inhomogeneous solver for which the homogeneous solver is a special case. This is valuable as, for nontrivial boundary perturbations, there are no exact solutions for plane–wave scattering.

As in [2], we select w which has the same "behavior" as solutions u of the homogeneous problem: We specify w such that $\mathcal{R}_w \equiv 0$. To be more specific, consider the functions

$$v_r^{(m)}(x,y) = A^{(m)} e^{i(\alpha_r \cdot x + \beta_r^{(m)} y)} + B^{(m)} e^{i(\alpha_r \cdot x - \beta_r^{(m)} y)}, \quad 0 \le m \le M, \tag{4.1}$$

with $r \in \mathbf{Z}$ and $A^{(M)} = B^{(0)} = 0$. These are outgoing, α–quasiperiodic solutions of the Helmholtz equation, so that $\mathcal{R}_w \equiv 0$ in the notation above. However, the boundary conditions satisfied by these functions are *not* those satisfied by an incident plane wave. With the construction of the $\mathcal{Q}_w$ in mind we compute the surface data

$$\begin{aligned} \tilde{\zeta}^{(m)} &:= v_r^{(m-1)} - v_r^{(m)} && y = \bar{g}^{(m)} + g^{(m)}(x), \quad 1 \le m \le M \\ \tilde{\psi}^{(m)} &:= \partial_{N^{(m)}} \left[v_r^{(m-1)} - v_r^{(m)} \right] && y = \bar{g}^{(m)} + g^{(m)}(x), \quad 1 \le m \le M. \end{aligned}$$

This is a family of exact solutions against which to test our numerical algorithm for *any* choice of deformations $\{g^{(1)}, \ldots, g^{(M)}\}$.

4.2. *Numerical implementation and error measurement.* We utilize Nyström's method [11] to simulate the integral equations (3.14) appearing in (2.3). In this setting this amounts to enforcing these equations at $N_x = (N_{x_1}, N_{x_2})$ equally spaced gridpoints, $x_j = (x_{1,j_1}, x_{2,j_2})$, on the period cell $[0, d_1] \times [0, d_2]$, with unknowns being the functions $\{\tilde{V}^{(m),l}, V^{(m),l}\}$ evaluated at these same gridpoints x_j.

To finish our discussion of the numerical implementation, we point out that one may choose among several methods to sum the truncated (at order N) Taylor series which

appear in our algorithm (see, e.g., (3.4)). In addition to simple direct (Taylor) summation, we have found that the classical numerical analytic continuation method of Padé approximation [3] has been very useful for HOPS methods in other contexts [7,30,31,34], and we use it here as well. The approximant has the remarkable property that, for a wide class of functions, not only is the convergence *faster* at points of analyticity but it also may converge for points *outside* the disk of convergence. We direct the interested reader to §2.2 of Baker and Graves–Morris [3] and the calculations in §8.3 of Bender and Orszag [4] for a complete discussion of the capabilities and limitations of Padé approximants.

With these approximations in hand we measure the error in our simulated solutions

$$V^{(m),l,N_x,N}(x;\varepsilon) := \sum_{n=0}^{N} \sum_{p=-N_x/2}^{N_x/2-1} \hat{V}_{p,n}^{(m)} e^{i\alpha_p \cdot x} \varepsilon^n,$$

$$\tilde{V}^{(m),l,N_x,N}(x;\varepsilon) := \sum_{n=0}^{N} \sum_{p=-N_x/2}^{N_x/2-1} \hat{\tilde{V}}_{p,n}^{(m)} e^{i\alpha_p \cdot x} \varepsilon^n,$$

versus the exact solutions (4.1), by computing the defect in the lower Dirichlet and Neumann traces. For the results described in §4.3 we measure

$$\epsilon_{rel} := \sup_{0\leq m\leq M-1} \left\{ \frac{\left|\tilde{V}_r^{(m),l} - \tilde{V}_r^{(m),l,N_x,N}\right|_{L^\infty}}{\left|\tilde{V}_r^{(m),l}\right|_{L^\infty}}, \frac{\left|V_r^{(m),l} - V_r^{(m),l,N_x N}\right|_{L^\infty}}{\left|V_r^{(m),l}\right|_{L^\infty}} \right\}. \tag{4.2}$$

4.3. *Convergence studies.* For our convergence studies we follow the developments in [2] and begin with two–dimensional and 2π–periodic profiles which are *independent* of the x_2–variable. Recall the three profiles introduced in [29] for precisely this purpose: The sinusoid

$$f_s(x) = \cos(x), \tag{4.3a}$$

the "rough" (C^4 but not C^5) profile

$$f_r(x) = \left(2 \times 10^{-4}\right) \left\{ x^4(2\pi - x)^4 - \frac{128\pi^8}{315} \right\}, \tag{4.3b}$$

and the Lipschitz boundary

$$f_L(x) = \begin{cases} -(2/\pi)x + 1, & 0 \leq x \leq \pi \\ (2/\pi)x - 3, & \pi \leq x \leq 2\pi. \end{cases} \tag{4.3c}$$

We point out that all three profiles have zero mean, approximate amplitude 2, and maximum slope of roughly 1. The Fourier series representations of f_r and f_L are listed in [29], and in order to minimize aliasing errors we approximate these by their truncated P–term Fourier series, $f_{r,P}$ and $f_{L,P}$, with $P = 40$.

We begin with the two three–layer configurations outlined in [2]:

(1) (Two Smooth Interfaces, Figure 2). Physical and numerical parameters:

$$\begin{gathered}\alpha = 0.1, \quad \beta^{(0)} = 1.1, \quad \beta^{(1)} = 2.2, \quad \beta^{(2)} = 3.3,\\ g^{(1)}(x) = \varepsilon f_s(x), \quad g^{(2)}(x) = \varepsilon f_s(x),\\ \varepsilon = 0.005, 0.01, 0.05, 0.1, \quad d = 2\pi,\\ N_x = 30, \quad N = 0, \ldots, 10. \end{gathered} \tag{4.4}$$

(2) (Rough and Lipschitz Interfaces, Figure 3). Physical and numerical parameters:

$$\begin{gathered}\alpha = 0.1, \quad \beta^{(0)} = 1.1, \quad \beta^{(1)} = 2.2, \quad \beta^{(2)} = 3.3,\\ g^{(1)}(x) = \varepsilon f_{r,40}(x), \quad g^{(2)}(x) = \varepsilon f_{L,40}(x),\\ \varepsilon = 0.001, 0.005, 0.01, 0.05, \quad d = 2\pi,\\ N_x = 320, \quad N = 0, \ldots, 10. \end{gathered} \tag{4.5}$$

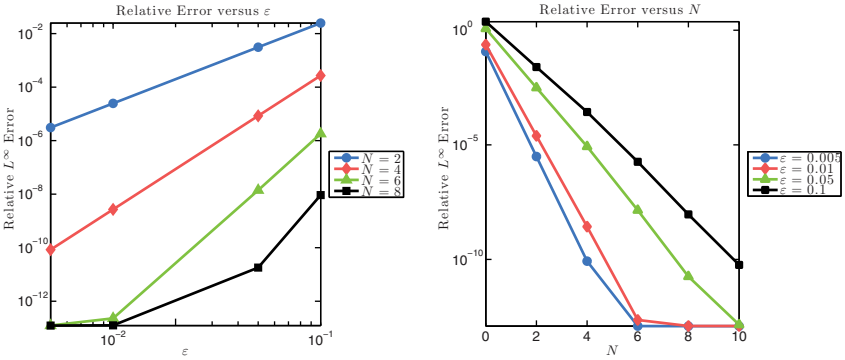

(a) Relative error versus ε (b) Relative error versus N

FIG. 2. (a) Relative error versus perturbation parameter ε for various perturbation orders N. (b) Relative error versus perturbation order N for various perturbation parameters ε. Results for the two–dimensional smooth–smooth configuration, (4.4), with $N_x = 30$.

By simulating (4.4), we demonstrate that a small number of quadrature points ($N_x \approx 30$) and perturbation orders ($N \approx 6$) are required to realize machine precision (up to the conditioning of our algorithm) for small (e.g., $\varepsilon = 0.01$), smooth profiles, (4.3a), which displays the spectral accuracy of the scheme. Configuration (4.5) tests our method in the case of lower and upper interfaces shaped by rough, (4.3b), and Lipschitz, (4.3c), profiles respectively (both truncated after $P = 40$ Fourier series terms) provided that N_x and N are chosen sufficiently large.

We choose two more representative configurations in the two–dimensional setting:

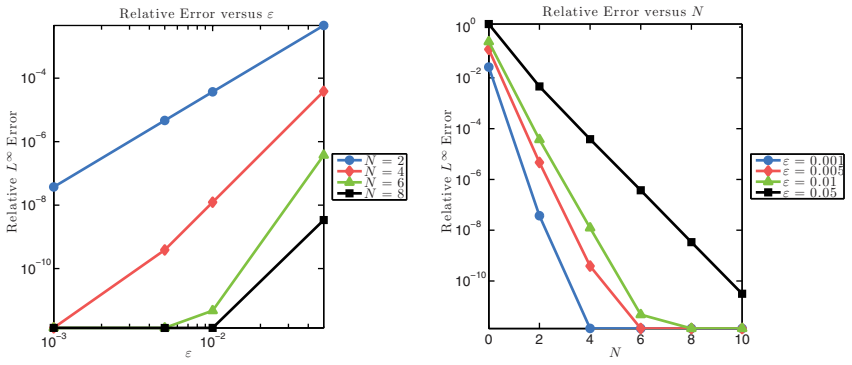

(a) Relative error versus ε (b) Relative error versus N

FIG. 3. (a) Relative error versus perturbation parameter ε for various perturbation orders N. (b) Relative error versus perturbation order N for various perturbation parameters ε. Results for the two–dimensional rough–Lipschitz configuration, (4.5), with $N_x = 320$.

(1) (Six–Layer, Figure 4). Physical and numerical parameters:

$$\begin{gathered}\alpha = 0.1, \quad \beta^{(m)} = 1.1 + m, \quad 0 \leq m \leq 5, \\ g^{(1)}(x) = \varepsilon f_s(x), \quad g^{(2)}(x) = \varepsilon f_{r,40}(x), \quad g^{(3)}(x) = \varepsilon f_{L,40}(x), \\ g^{(4)}(x) = \varepsilon f_{r,40}(x), \quad g^{(5)}(x) = \varepsilon f_s(x), \\ \varepsilon = 0.001, 0.005, 0.01, 0.05, \quad d = 2\pi, \\ N_x = 120, \quad N = 0, \ldots, 10. \end{gathered} \tag{4.6}$$

(2) (21–Layer, Figure 5). Physical and numerical parameters:

$$\begin{gathered}\alpha = 0.1, \quad \beta^{(m)} = \frac{m+1}{10}, \quad 0 \leq m \leq 20, \\ g^{(m)}(x) = \varepsilon f_s(x), \quad 1 \leq m \leq 20, \\ \varepsilon = 0.001, 0.005, 0.01, 0.05, \quad d = 2\pi, \\ N_x = 30, \quad N = 0, \ldots, 10. \end{gathered} \tag{4.7}$$

Again, our algorithm provides highly accurate solutions in a stable and rapid manner provided that a sufficient number of quadrature points, N_x, and perturbation orders, N, are retained.

We now move to the more general case of $(2\pi) \times (2\pi)$ periodic interfaces in a three–dimensional structure. Again, we follow [2] and select the following interface shapes: The sinusoid

$$\tilde{f}_s(x_1, x_2) = \cos(x_1 + x_2), \tag{4.8a}$$

the "rough" (C^2 but not C^3) profile

$$\tilde{f}_r(x_1, x_2) = \left(\frac{2}{9} \times 10^{-3}\right) \left\{ x_1^2 (2\pi - x_1)^2 x_2^2 (2\pi - x_2)^2 - \frac{64\pi^8}{225} \right\}, \tag{4.8b}$$

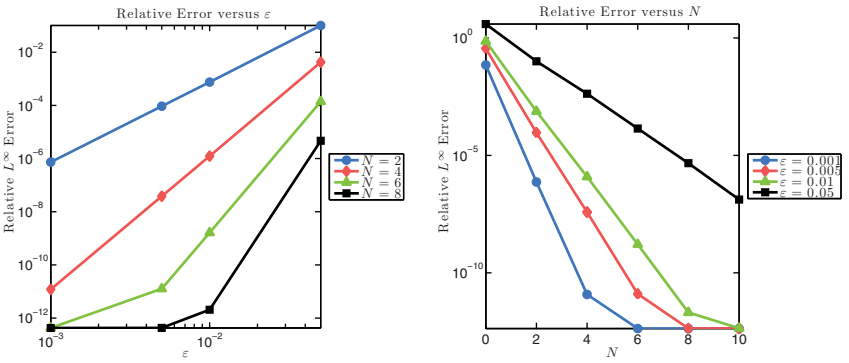

(a) Relative error versus ε (b) Relative error versus N

FIG. 4. (a) Relative error versus perturbation parameter ε for various perturbation orders N. (b) Relative error versus perturbation order N for various perturbation parameters ε. Results for the two–dimensional smooth–rough–Lipschitz–rough–smooth configuration, (4.6), with $N_x = 120$.

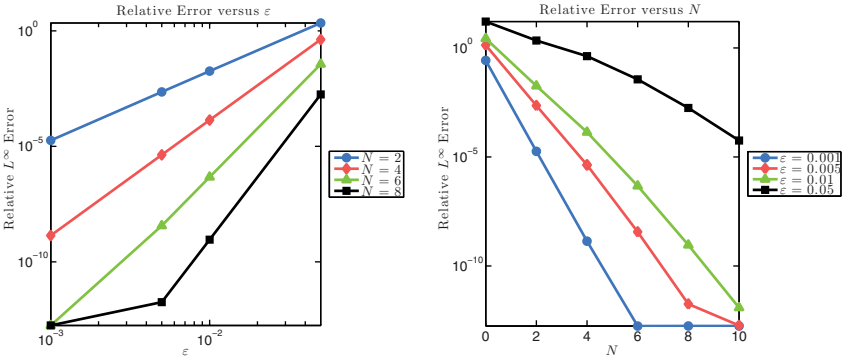

(a) Relative error versus ε (b) Relative error versus N

FIG. 5. (a) Relative error versus perturbation parameter ε for various perturbation orders N. (b) Relative error versus perturbation order N for various perturbation parameters ε. Results for the two–dimensional 21–layer configuration, (4.7), with $N_x = 30$.

and the Lipschitz boundary

$$\tilde{f}_L(x_1, x_2) = \frac{1}{3} + \begin{cases} -1 + (2/\pi)x_1, & x_1 \le x_2 \le 2\pi - x_1 \\ 3 - (2/\pi)x_2, & x_2 > x_1,\ x_2 > 2\pi - x_1 \\ 3 - (2/\pi)x_1, & 2\pi - x_1 < x_2 < x_1 \\ -1 + (2/\pi)x_2, & x_2 < x_1,\ x_2 < 2\pi - x_1. \end{cases} \tag{4.8c}$$

Again, all three profiles have zero mean, approximate amplitude 2, and maximum slope of roughly 1. The Fourier series representations of $\tilde{f}_r$ and $\tilde{f}_L$ are given in [29] and in

order to minimize aliasing errors we approximate these by their truncation after $P = 20$ coefficients, $\tilde{f}_{r,P}$ and $\tilde{f}_{L,P}$.

We now consider two three–layer configurations outlined below.

(1) (Two smooth interfaces, Figure 6). Physical and numerical parameters:

$$\alpha_1 = 0.1, \quad \alpha_2 = 0.2, \quad \beta^{(0)} = 1.1, \quad \beta^{(1)} = 2.2, \quad \beta^{(2)} = 3.3,$$
$$g^{(1)}(x_1, x_2) = \varepsilon \tilde{f}_s(x_1, x_2), \quad g^{(2)}(x_1, x_2) = \varepsilon \tilde{f}_s(x_1, x_2),$$
$$\varepsilon = 0.005, 0.01, 0.05, 0.1, \quad d_1 = 2\pi, \quad d_2 = 2\pi,$$
$$N_{x_1} = N_{x_2} = 24, \quad N = 0, \ldots, 10. \tag{4.9}$$

(2) (Rough and Lipschitz interfaces, Figure 7). Physical and numerical parameters:

$$\alpha_1 = 0.1, \quad \alpha_2 = 0.2, \quad \beta^{(0)} = 1.1, \quad \beta^{(1)} = 2.2, \quad \beta^{(2)} = 3.3,$$
$$g^{(1)}(x_1, x_2) = \varepsilon \tilde{f}_{r,20}(x_1, x_2), \quad g^{(2)}(x_1, x_2) = \varepsilon \tilde{f}_{L,20}(x_1, x_2),$$
$$\varepsilon = 0.001, 0.005, 0.01, 0.05, \quad d_1 = 2\pi, \quad d_2 = 2\pi,$$
$$N_{x_1} = N_{x_2} = 64, \quad N = 0, \ldots, 10. \tag{4.10}$$

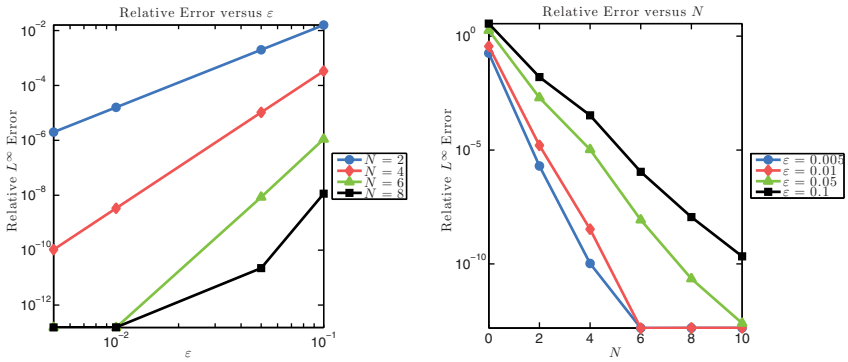

(a) Relative error versus ε (b) Relative error versus N

FIG. 6. (a) Relative error versus perturbation parameter ε for various perturbation orders N. (b) Relative error versus perturbation order N for various perturbation parameters ε. Results for the three–dimensional smooth–smooth configuration, (4.9), with $N_{x_1} = N_{x_2} = 24$.

Again, our algorithm produces highly accurate results in a stable and reliable manner. The behavior is independent of interface shape provided that a sufficient number of quadrature points and perturbation orders are used.

4.4. *Layered medium simulations.* Having verified the validity of our codes, we demonstrate the utility of our approach by simulating *plane–wave* scattering from the configurations described in the previous section. For this there is no exact solution for comparison, so we resort to our diagnostic of energy defect (3.19).

We observe in Figure 8 that we achieve full double precision accuracy with merely $N = 6$ perturbation orders for the smooth–smooth configuration ($\varepsilon = 0.005, 0.01$), (4.4), while in Figure 9 we show that the same can be realized for the rough–Lipschitz problem,

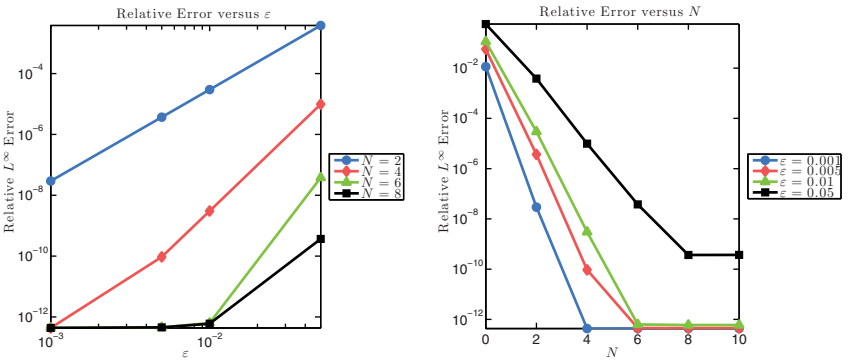

(a) Relative error versus ε (b) Relative error versus N

FIG. 7. (a) Relative error versus perturbation parameter ε for various perturbation orders N. (b) Relative error versus perturbation order N for various perturbation parameters ε. Results for the three–dimensional rough–Lipschitz configuration, (4.10), with $N_{x_1} = N_{x_2} = 64$.

(4.5). We note the same behavior for the six–layer configuration, (4.6), and the 21–layer device, (4.7), which are displayed in Figures 10 and 11, respectively. Finally, we display three–dimensional results corresponding to the three–layer problems, (4.9) and (4.10), and the quantitative results are given in Figures 12 and 13, respectively.

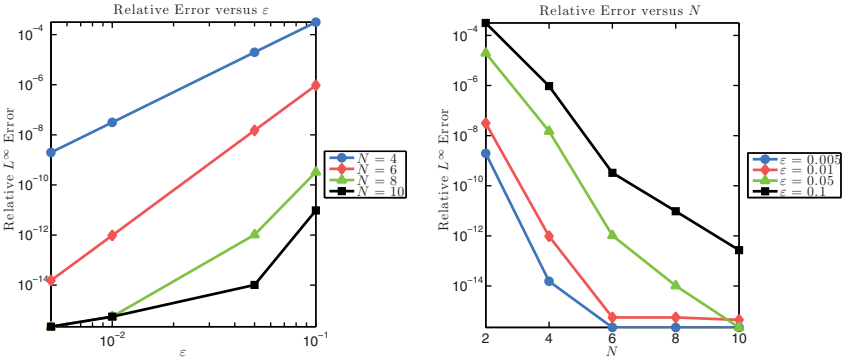

(a) Energy defect versus ε (b) Energy defect versus N

FIG. 8. (a) Energy defect versus perturbation parameter ε for various perturbation orders N. (b) Energy defect versus perturbation order N for various perturbation parameters ε. Results for the two–dimensional smooth–smooth configuration, (4.4), with $N_x = 30$.

4.5. *Layered media simulations requiring the new algorithm.* We close with simulations which *mandate* the use of our new approach due to the enormous conditioning and speed advantages that our novel HOPS algorithm can exhibit in comparison with the "Direct"

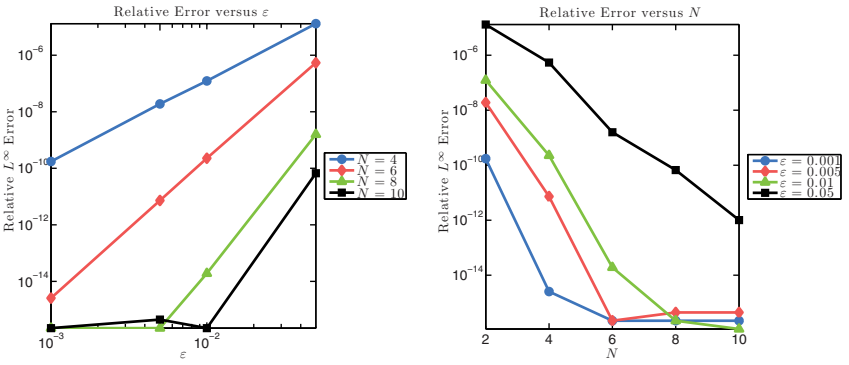

(a) Energy defect versus ε (b) Energy defect versus N

FIG. 9. (a) Energy defect versus perturbation parameter ε for various perturbation orders N. (b) Energy defect versus perturbation order N for various perturbation parameters ε. Results for the two–dimensional rough–Lipschitz configuration, (4.5), with $N_x = 320$.

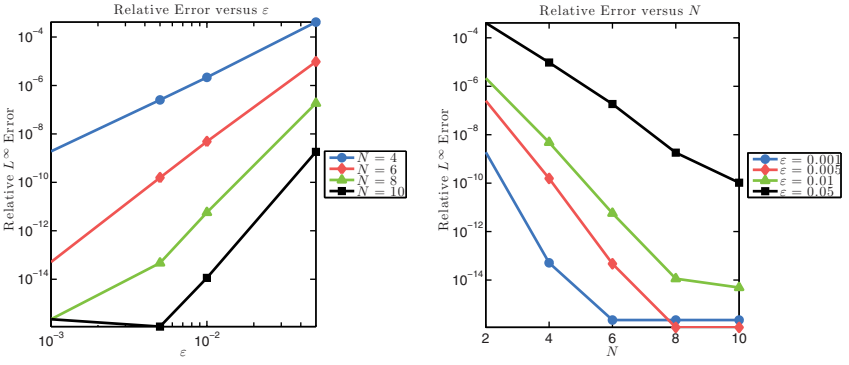

(a) Energy defect versus ε (b) Energy defect versus N

FIG. 10. (a) Energy defect versus perturbation parameter ε for various perturbation orders N. (b) Energy defect versus perturbation order N for various perturbation parameters ε. Results for the two–dimensional smooth–rough–Lipschitz–rough–smooth configuration, (4.6), with $N_x = 120$.

approach advocated in [2]. To guide this discussion we recall three noteworthy aspects of our new recursions:

(1) Whereas the "Direct" method of [2] entails the inversion of the operator $\hat{A}_p(g)$ in (2.4), our recursive HOPS method requires the (repeated) inversion of $\hat{A}_{p,0} = \hat{A}_p(0)$. Not only can this be accomplished *rapidly* (via an FFT [15] with cost $\mathcal{O}(N_x \log(N_x))$), this operator is much better conditioned.

(2) The operators $\hat{A}_{n,p}$ can be seen to be the composition of physical products and convolution integrals (see steps 1–3) which can be stably and rapidly (again,

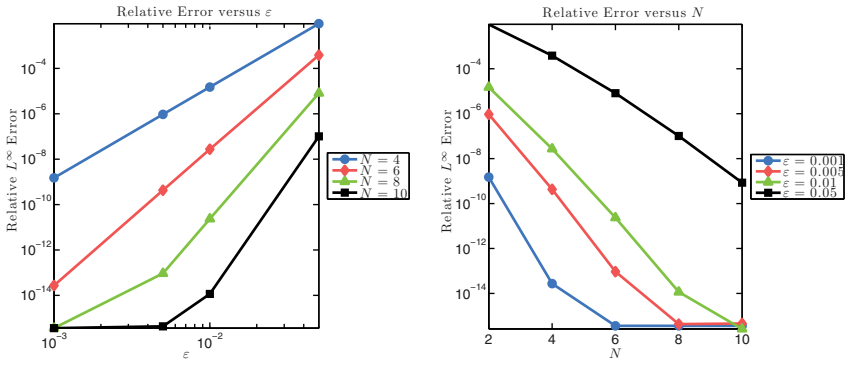

(a) Energy defect versus ε (b) Energy defect versus N

FIG. 11. (a) Energy defect versus perturbation parameter ε for various perturbation orders N. (b) Energy defect versus perturbation order N for various perturbation parameters ε. Results for the two–dimensional 21–layer configuration, (4.7), with $N_x = 30$.

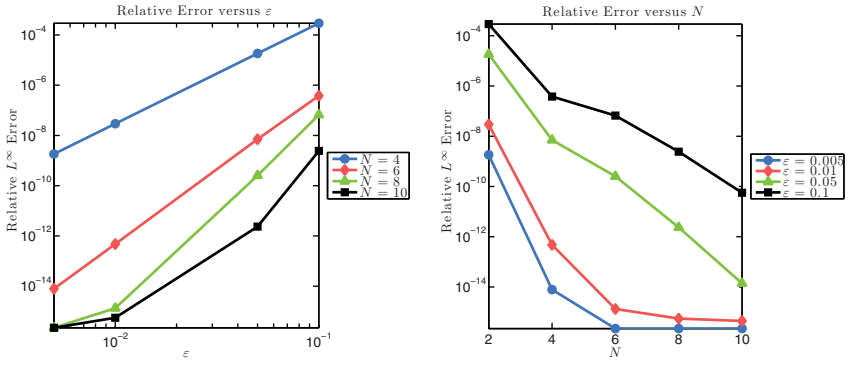

(a) Energy defect versus ε (b) Energy defect versus N

FIG. 12. (a) Energy defect versus perturbation parameter ε for various perturbation orders N. (b) Energy defect versus perturbation order N for various perturbation parameters ε. Results for the three–dimensional smooth–smooth configuration, (4.9), with $N_{x_1} = N_{x_2} = 24$.

via FFT) evaluated. By contrast, $\hat{A}_p(g)$ has no such structure, and a direct application strategy will cost $\mathcal{O}(N_x^2)$, while inversion takes time $\mathcal{O}(N_x^3)$.

(3) Our HOPS approach admits the possibility of alternate summation mechanisms such as Padé approximation [3] which have their own remarkable properties of accuracy and stability enhancement.

To illustrate these points we now revisit the two–dimensional, smooth–smooth configuration (4.4), but now with much larger values of the deformation amplitude $\varepsilon = 0.1, 0.15, 0.2, 0.25$. Due to these much larger perturbations, many more Taylor orders ($N \approx 30$) are required for well–resolved solutions. Correspondingly, as the n–th order

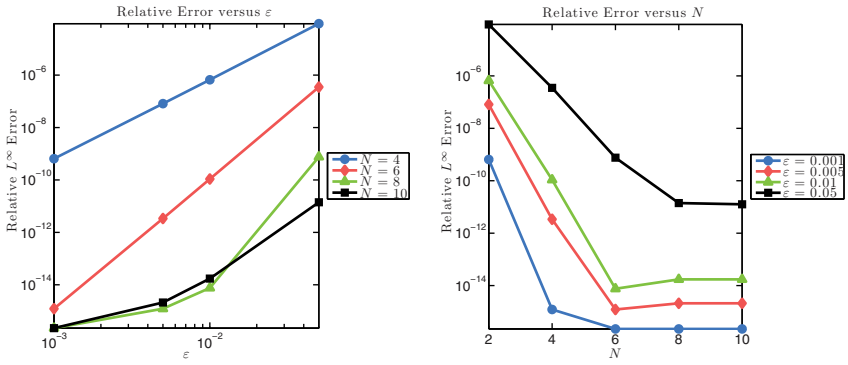

(a) Energy defect versus ε (b) Energy defect versus N

FIG. 13. (a) Energy defect versus perturbation parameter ε for various perturbation orders N. (b) Energy defect versus perturbation order N for various perturbation parameters ε. Results for the three–dimensional rough–Lipschitz configuration, (4.10), with $N_x = 30$.

correction requires the n–th power of $f(x)$ (see, e.g., (3.8)) this demands many more quadrature points (we use $N_x = 200$) to realize high–order accuracy.

We begin with point 1 and display in Figure 14(a) estimates of the condition number of $A(g)$ and $A(0)$ versus number of quadrature points N_x using MATLAB's `cond` command [23]. While this quantity grows for $A(0)$, the rate is extremely slow and certainly dwarfed by the catastrophic growth displayed by $A(g)$. One consequence of this characteristic is the deteriorating accuracy of the Direct method as the number of quadrature points is increased (see Figure 14(b)), which is the hallmark of an ill–conditioned algorithm. This is compared to our new algorithm with the Padé summation algorithm utilized.

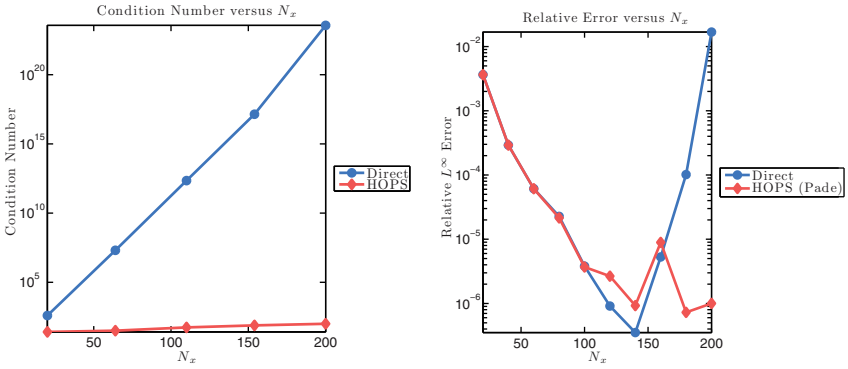

(a) Condition number versus N_x (b) Relative error versus N_x

FIG. 14. (a) Condition number versus N_x for Direct and HOPS methods. (b) Relative error versus N_x for Direct and HOPS (Padé summation, $N = 30$) methods. Results for the two–dimensional smooth–smooth configuration, (4.4).

Regarding point 2, in Figure 15 we plot timings (scaled by the time of a HOPS simulation with $N_x = 200$ and $N = 30$) of the Direct method and our new HOPS approach as the number of quadrature points is increased. Here the great advantage in speed of our new approach is on display, which enables the high–order approximation of configurations of interest with our new, well–conditioned approach. Due to the large number of perturbation orders ($N = 30$) computed, the Direct approach (independent of N) is quicker for N_x very small; however, as N_x is increased this advantage quickly evaporates, and the onerous cost of the Direct method overwhelms our rapid new algorithm.

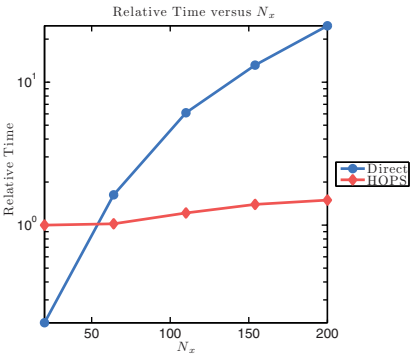

FIG. 15. Relative elapsed time versus N_x for Direct and HOPS methods. Results for the two–dimensional smooth–smooth configuration, (4.4).

To close, we turn to point 3 and display, in Figures 16 and 17, results comparing the performance of Taylor summation versus Padé approximation. We note from Figure 16(a) that with Taylor summation, one always realizes better results for larger values of N provided that it is not chosen too large. However, as Figure 16(b) shows, this does not hold uniformly over all perturbation orders, and, as N is increased, a certain ill–conditioning sets in, which has been noticed for other HOPS methods (see [28–30]). On the other hand, as we show in Figure 17, while not solving the underlying issues explicitly, Padé summation is able to ameliorate these problems and return simulations which are both robust and highly accurate. The effect becomes more pronounced for large values of N and/or ε, meaning that with this "Padé enhancement" we have the capability to simulate configurations of large size and severe roughness.

We conclude with the results of a simulation which demonstrate a final advantage of our new HOPS scheme which we mentioned earlier, namely the ability to simulate scattering returns from an entire *family* of profiles in a single computation. In Figure 18 we display, for the two–dimensional smooth–smooth configuration (4.4), the specular (order zero) efficiencies in the upper–most, $B_0^{(0)}$, and lower–most, $B_0^{(M)}$, layers as a function of the deformation size, ε. While this plot could have easily been generated with the Direct approach, the 101 data points displayed here would have required 101 simulations. By comparison, a single HOPS simulation followed by simple post–processing with negligible cost produced this plot. Furthermore, if further investigation merits the evaluation at *any* intermediate value, this can be accomplished with very little extra effort.

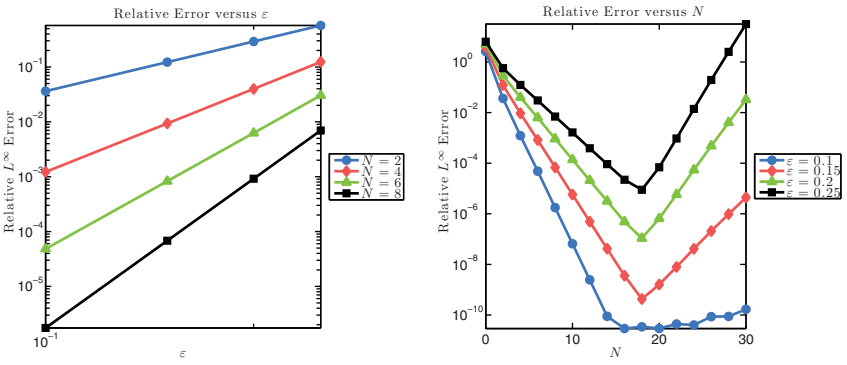

(a) Relative error versus ε (b) Relative error versus N

FIG. 16. (a) Relative error versus perturbation parameter ε for various perturbation orders N. (b) Relative error versus perturbation order N for various perturbation parameters ε. Results for the two–dimensional smooth–smooth configuration, (4.4), with $N_x = 200$ and Taylor summation.

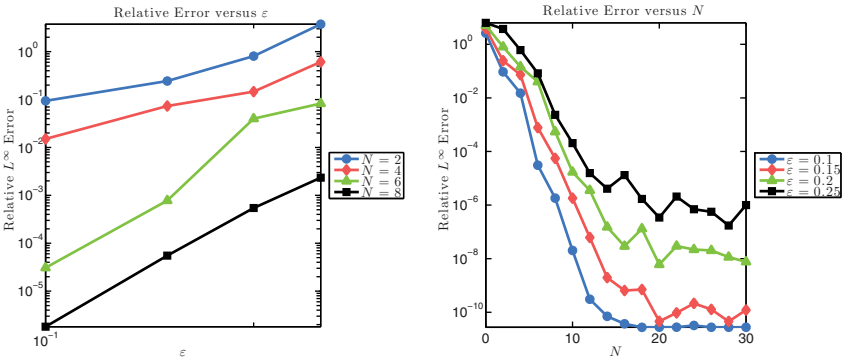

(a) Energy defect versus ε (b) Energy defect versus N

FIG. 17. (a) Energy defect versus perturbation parameter ε for various perturbation orders N. (b) Energy defect versus perturbation order N for various perturbation parameters ε. Results for the two–dimensional smooth–smooth configuration, (4.4), with $N_x = 200$ and Padé summation.

Dedication. My time as a graduate student in the Division of Applied Mathematics at Brown University was profoundly important for me both scientifically and personally. Many people contributed to this and among these was Dimpy Pathria, who was in Applied Math as a post–doctoral fellow while I was there. Among other things, she taught a Methods of Applied Mathematics course, which, though I only audited, proved to be invaluable to me. In the fall of 2011 she suddenly fell quite ill and mere months later passed away. The first seeds of an idea which resulted in the algorithm described in this paper were planted during this time, so I would like to dedicate this paper to her

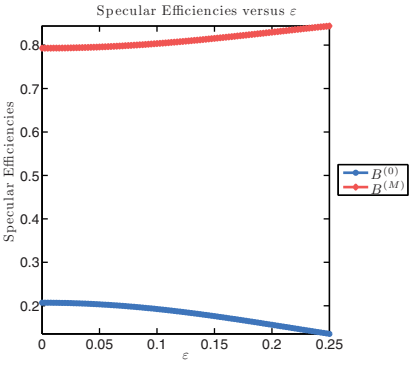

FIG. 18. Specular efficiencies versus ε computed by our HOPS algorithm with Padé summation ($N_x = 200$ and $N = 30$) for the two–dimensional smooth–smooth configuration, (4.4).

memory. She was not only the loving wife of my good friend Paul Fischer and wonderful mother to Rita, but she was also a friend and mentor to many in the Brown Applied Math family. Her influence will be felt by many for years to come.

Acknowledgments. The author gratefully acknowledges support from the National Science Foundation through grant No. DMS–1115333.

REFERENCES

[1] M. J. Ablowitz, A. S. Fokas, and Z. H. Musslimani, *On a new non-local formulation of water waves*, J. Fluid Mech. **562** (2006), 313–343, DOI 10.1017/S0022112006001091. MR2263547 (2007k:76013)

[2] David M. Ambrose and David P. Nicholls, *Fokas integral equations for three dimensional layered-media scattering*, J. Comput. Phys. **276** (2014), 1–25, DOI 10.1016/j.jcp.2014.07.018. MR3252567

[3] George A. Baker Jr. and Peter Graves-Morris, *Padé approximants*, 2nd ed., Encyclopedia of Mathematics and its Applications, vol. 59, Cambridge University Press, Cambridge, 1996. MR1383091 (97h:41001)

[4] Carl M. Bender and Steven A. Orszag, *Advanced mathematical methods for scientists and engineers*, International Series in Pure and Applied Mathematics, McGraw-Hill Book Co., New York, 1978. MR538168 (80d:00030)

[5] Florian Bleibinhaus and Stéphane Rondenay, *Effects of surface scattering in full-waveform inversion*, Geophysics **74**(6):WCC69–WCC77, 2009.

[6] L. M. Brekhovskikh and Yu. P. Lysanov, *Fundamentals of ocean acoustics*, 2nd ed., Springer Series on Wave Phenomena, vol. 8, Springer-Verlag, Berlin, 1991. MR1100922 (93a:76086)

[7] Oscar P. Bruno and Fernando Reitich, *Numerical solution of diffraction problems: A method of variation of boundaries*, J. Opt. Soc. Am. A **10**(6):1168–1175, 1993.

[8] Oscar P. Bruno and Fernando Reitich, *Numerical solution of diffraction problems: A method of variation of boundaries. II. Finitely conducting gratings, Padé approximants, and singularities*, J. Opt. Soc. Am. A **10**(11):2307–2316, 1993.

[9] Oscar P. Bruno and Fernando Reitich, *Numerical solution of diffraction problems: A method of variation of boundaries. III. Doubly periodic gratings*, J. Opt. Soc. Am. A **10**(12):2551–2562, 1993.

[10] R. Coifman, M. Goldberg, T. Hrycak, M. Israeli, and V. Rokhlin, *An improved operator expansion algorithm for direct and inverse scattering computations*, Waves Random Media **9** (1999), no. 3, 441–457, DOI 10.1088/0959-7174/9/3/311. MR1705850 (2000f:65151)

[11] David Colton and Rainer Kress, *Inverse acoustic and electromagnetic scattering theory*, 2nd ed., Applied Mathematical Sciences, vol. 93, Springer-Verlag, Berlin, 1998. MR1635980 (99c:35181)

[12] T. Ebbesen, H. Lezec, H. Ghaemi, T. Thio, and P. Wolff, *Extraordinary optical transmission through sub-wavelength hole arrays*, Nature **391**(6668):667–669, 1998.

[13] Athanassios S. Fokas, *A unified approach to boundary value problems*, CBMS-NSF Regional Conference Series in Applied Mathematics, vol. 78, Society for Industrial and Applied Mathematics (SIAM), Philadelphia, PA, 2008. MR2451953 (2010b:35038)

[14] L. Geli, P. Y. Bard, and B. Jullien, *The effect of topography on earthquake ground motion: a review and new results*, Bulletin of the Seismological Society of America **78**(1):42–63, 1988.

[15] David Gottlieb and Steven A. Orszag, *Numerical analysis of spectral methods: theory and applications*, CBMS-NSF Regional Conference Series in Applied Mathematics, No. 26, Society for Industrial and Applied Mathematics, Philadelphia, Pa., 1977. MR0520152 (58 #24983)

[16] L. Greengard and V. Rokhlin, *A fast algorithm for particle simulations*, J. Comput. Phys. **73** (1987), no. 2, 325–348, DOI 10.1016/0021-9991(87)90140-9. MR918448 (88k:82007)

[17] J. Homola, *Surface plasmon resonance sensors for detection of chemical and biological species*, Chemical Reviews **108**(2):462–493, 2008.

[18] D. Komatitsch and J. Tromp, *Spectral-element simulations of global seismic wave propagation-I. Validation*, Geophysical Journal International **149**(2):390–412, 2002.

[19] Harun Kurkcu and Fernando Reitich, *Stable and efficient evaluation of periodized Green's functions for the Helmholtz equation at high frequencies*, J. Comput. Phys. **228** (2009), no. 1, 75–95, DOI 10.1016/j.jcp.2008.08.021. MR2464068 (2009j:35005)

[20] Nathan C. Lindquist, Timothy W. Johnson, Jincy Jose, Lauren M. Otto, and Sang-Hyun Oh, *Ultrasmooth metallic films with buried nanostructures for backside reflection-mode plasmonic biosensing*, Annalen der Physik **524**:687–696, 2012.

[21] Alison Malcolm and David P. Nicholls, *A boundary perturbation method for recovering interface shapes in layered media*, Inverse Problems **27** (2011), no. 9, 095009, 18, DOI 10.1088/0266-5611/27/9/095009. MR2831891 (2012e:65246)

[22] Alison Malcolm and David P. Nicholls, *A field expansions method for scattering by periodic multilayered media*, Journal of the Acoustical Society of America **129**(4):1783–1793, 2011.

[23] MATLAB, *version 7.10.0 (R2010a)*, The MathWorks Inc., Natick, Massachusetts, 2010.

[24] D. Michael Milder, An improved formalism for rough-surface scattering of acoustic and electromagnetic waves, in *Proceedings of SPIE - The International Society for Optical Engineering (San Diego, 1991)*, volume 1558, Int. Soc. for Optical Engineering, Bellingham, WA, 1991, pp. 213–221.

[25] D. Michael Milder, *An improved formalism for wave scattering from rough surfaces*, J. Acoust. Soc. Am. **89**(2):529–541, 1991.

[26] M. Moskovits, *Surface–enhanced spectroscopy*, Reviews of Modern Physics **57**(3):783–826, 1985.

[27] David P. Nicholls, *Three-dimensional acoustic scattering by layered media: a novel surface formulation with operator expansions implementation*, Proc. R. Soc. Lond. Ser. A Math. Phys. Eng. Sci. **468** (2012), no. 2139, 731–758, DOI 10.1098/rspa.2011.0555. MR2892310

[28] David P. Nicholls and Fernando Reitich, *A new approach to analyticity of Dirichlet-Neumann operators*, Proc. Roy. Soc. Edinburgh Sect. A **131** (2001), no. 6, 1411–1433, DOI 10.1017/S0308210500001463. MR1869643 (2003b:35216)

[29] David P. Nicholls and Fernando Reitich, *Stability of high-order perturbative methods for the computation of Dirichlet-Neumann operators*, J. Comput. Phys. **170** (2001), no. 1, 276–298, DOI 10.1006/jcph.2001.6737. MR1843612 (2002c:65234)

[30] David P. Nicholls and Fernando Reitich, *Analytic continuation of Dirichlet-Neumann operators*, Numer. Math. **94** (2003), no. 1, 107–146, DOI 10.1007/s002110200399. MR1971215 (2004b:65164)

[31] D. P. Nicholls, F. Reitich, T. Johnson, and S.-H. Oh, *Fast high–order perturbation of surfaces (HOPS) methods for simulation of multi–layer plasmonic devices and metamaterials*, Journal of Optical Society of America, A, Volume 31, Issue 8, 1820–1831, 2014.

[32] *Electromagnetic theory of gratings,* edited by Roger Petit, Topics in Current Physics, vol. 22, Springer-Verlag, Berlin-New York, 1980. MR609533 (82a:78001)

[33] R. Gerhard Pratt, *Frequency-domain elastic wave modeling by finite differences: A tool for crosshole seismic imaging*, Geophysics **55**(5):626–632, 1990.

[34] F. Reitich, T. Johnson, S.-H. Oh, and G. Meyer, *A fast and high-order accurate boundary perturbation method for characterization and design in nanoplasmonics*, Journal of the Optical Society of America, A **30**:2175, 2013.

[35] F. Reitich and K. K. Tamma, *State-of-the-art, trends, and directions in computational electromagnetics [Special issue on computational electromagnetics]*, CMES Comput. Model. Eng. Sci. **5** (2004), no. 4, 287–294. MR2070390

[36] F. J. Sanchez-Sesma, V. J. Palencia, and F. Luzon, Estimation of local site effects during earthquakes: An overview, in V. K. Gupta, editor, from *Seismic Source to Structural Response*, University of Southern California, Department of Civil Engineering, 2004, pp. 44–70.

[37] F. J. Sanchez-Sesma, E. Perez-Rocha, and S. Chavez-Perez, *Diffraction of elastic waves by three-dimensional surface irregularities. Part II*, Bulletin of the Seismological Society of America **79**(1):101–112, 1989.

[38] Peter J. Shull, *Nondestructive Evaluation: Theory, Techniques, and Applications*, Marcel Dekker, 2002.

[39] E. A. Spence and A. S. Fokas, *A new transform method I: domain-dependent fundamental solutions and integral representations*, Proc. R. Soc. Lond. Ser. A Math. Phys. Eng. Sci. **466** (2010), no. 2120, 2259–2281, DOI 10.1098/rspa.2009.0512. MR2659494 (2011e:35004)

[40] E. A. Spence and A. S. Fokas, *A new transform method II: the global relation and boundary-value problems in polar coordinates*, Proc. R. Soc. Lond. Ser. A Math. Phys. Eng. Sci. **466** (2010), no. 2120, 2283–2307, DOI 10.1098/rspa.2009.0513. MR2659495 (2011f:35008)

[41] L. Tsang, J. A. Kong, and R. T. Shin, *Theory of Microwave Remote Sensing*, Wiley, New York, 1985.

[42] J. Virieux and S. Operto, *An overview of full-waveform inversion in exploration geophysics*, Geophysics **74**(6):WCC1–WCC26, 2009.

[43] O. C. Zienkiewicz, *The finite element method in engineering science*, The second, expanded and revised, edition of *The finite element method in structural and continuum mechanics*, McGraw-Hill, London-New York-Düsseldorf, 1971. MR0315970 (47 #4518)